Electronic Supplementary Information

Self-Consistent Field Theory and Coarse-Grained Molecular Dynamics Simulations of Pentablock Copolymer Melt Phase Behavior

So Jung Park,[§a] Tristan Myers,[§a] Vinson Liao,[a] Arthi Jayaraman*[a,b,c]

a. *Department of Chemical and Biomolecular Engineering, University of Delaware, Colburn Lab,*
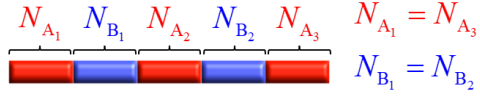
    150 Academy Street, Newark, DE 19716

b. *Department of Materials Science and Engineering, University of Delaware, Newark DE*

c. *Data Science Institute, University of Delaware, Newark DE*

* Corresponding author arthij@udel.edu

[§] S.J.P. and T.M. contributed equally to the article

a. $A_1B_1A_2B_2A_3$ **pentablock**   **b.** $B_1A_1B_2A_2B_3$ **pentablock**

N_{A_1} N_{B_1} N_{A_2} N_{B_2} N_{A_3} $N_{A_1} = N_{A_3}$
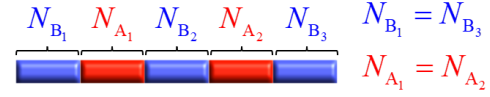
$N_{B_1} = N_{B_2}$

$$N = \sum_{i=1}^{3} N_{A_i} + \sum_{i=1}^{2} N_{B_i}$$

Polymer Design Parameters:

$$f_A \equiv \left(\sum_{i=1}^{3} N_{A_i} \right) / N$$

$$\tau_{A_2} \equiv N_{A_2} / \left(\sum_{i=1}^{3} N_{A_i} \right)$$

N_{B_1} N_{A_1} N_{B_2} N_{A_2} N_{B_3} $N_{B_1} = N_{B_3}$

$N_{A_1} = N_{A_2}$

$$N = \sum_{i=1}^{2} N_{A_i} + \sum_{i=1}^{3} N_{B_i}$$

Polymer Design Parameters:

$$f_A \equiv \left(\sum_{i=1}^{2} N_{A_i} \right) / N$$

$$\tau_{B_2} \equiv N_{B_2} / \left(\sum_{i=1}^{3} N_{B_i} \right)$$

*Fig. S1 (**Same as Figure 1 in the main manuscript**) Schematics of (a) symmetric $A_1B_1A_2B_2A_3$ pentaBCP and (b) symmetric $B_1A_1B_2A_2B_3$ pentaBCP, where N_γ is degree of polymerization of γ type block in the polymer chain ((a) $\gamma = \{A_1, B_1, A_2, B_2, A_3\}$, and (b) $\gamma = \{B_1, A_1, B_2, A_2, B_3\}$), and the A and B monomers have the same monomer volume. The polymer design parameters for each pentaBCP are defined below the schematics. The f_A is the overall volume fraction of A blocks in the polymer chain, and τ_{A_2} is the volume fraction of the middle A_2 block to the total A blocks for the $A_1B_1A_2B_2A_3$ pentaBCP, and τ_{B_2} is the volume fraction of the middle B_2 block to the total B blocks for the $B_1A_1B_2A_2B_3$ pentaBCP.*
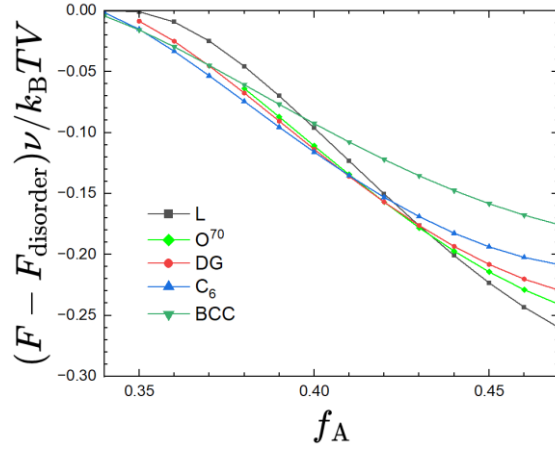
Fig. S2 *Relative free energies per segment (free energies per chain of length N) to the homogeneous disordered phase for the lamellae (L), double gyroid (DG), Fddd orthorhombic network (O^{70}), hexagonal-packed cylinder (C$_6$), and body-centered cubic sphere (BCC) phases in the A$_1$B$_1$A$_2$B$_2$A$_3$ pentaBCP melts at $\chi N = 40$ and $\tau_{A_2} = 0.5$.*

Table S1 *The end-to-end distance from MD* R_{ee}^{MD}*, SCFT unit cell parameter* C_{uc}^{SCFT}*, the real-space length* L_{q*} *equivalent to the q* peak of the A domain structure factor, and the MD unit cell parameter* C_{uc}^{MD}*. The* R_{ee}^{MD} *are sampled in the first simulation protocol at* $\chi N = 60$ *for each chain in the frames sampled from all three trials of each chain design. The* C_{uc}^{SCFT} *are given for the morphology predicted by SCFT at* $\chi N = 60$*. The* L_{q*} *are sampled in the second simulation protocol at* $\chi N = 120$ *from all sampled frames across three trials per chain design. The* C_{uc}^{MD}*, found as the quotient of* L_{q*} *and* R_{ee}^{MD}*, are provided for comparison with* C_{uc}^{SCFT}*.* R_{ee}^{MD} *and* C_{uc}^{SCFT} *are used to specify* L_{uc} *for the second simulation protocol, and* L_{q*} *is used to specify the simulation scale for the third simulation protocol. For both sampled quantities, the standard deviation is given as the error.*

$A_1B_1A_2B_2A_3, f_A \sim 0.33$					
τ_{A_2}	0.18	0.41	0.53	0.65	0.76
R_{ee}^{MD} (σ)	8.9 ± 3.6	8.8 ± 3.6	8.9 ± 3.5	8.9 ± 3.6	9.1 ± 3.6
C_{uc}^{SCFT}	1.2	1.0	0.9	1.0	1.2
L_{q*}	11.3 ± 0.0	9.3 ± 0.0	9.7 ± 0.2	9.5 ± 0.2	10.4 ± 0.0
C_{uc}^{MD}	1.3	1.1	1.1	1.1	1.1

$A_1B_1A_2B_2A_3, f_A \sim 0.40$					
τ_{A_2}	0.2	0.4	0.5	0.6	0.8
R_{ee}^{MD} (σ)	8.8 ± 3.6	8.8 ± 3.6	8.8 ± 3.6	8.9 ± 3.6	9.0 ± 3.6
C_{uc}^{SCFT}	1.1	0.8	0.8	2.1	1.2
L_{q*}	10.5 ± 0.2	9.4 ± 0.0	9.7 ± 0.2	9.7 ± 0.2	10.8 ± 0.2
C_{uc}^{MD}	1.2	1.1	1.1	1.1	1.2

$B_1A_1B_2A_2B_3, f_A \sim 0.33$					
τ_{A_2}	0.19	0.38	0.50	0.63	0.81
R_{ee}^{MD} (σ)	8.5 ± 3.4	8.5 ± 3.4	8.6 ± 3.5	8.6 ± 3.4	8.6 ± 3.4
C_{uc}^{SCFT}	0.9	0.9	0.9	2.0	0.9
L_{q*}	10.7 ± 0.4	9.2 ± 0.0	9.1 ± 0.2	9.2 ± 0.0	10.8 ± 0.2
C_{uc}^{MD}	1.3	1.1	1.1	1.1	1.3

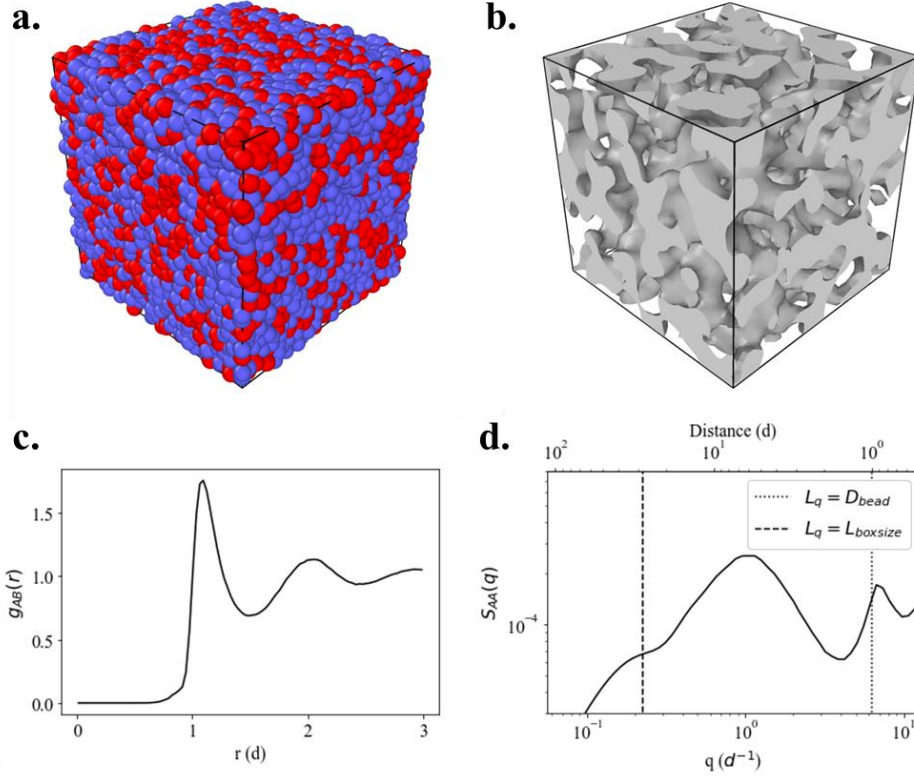| $B_1A_1B_2A_2B_3, f_A \sim 0.39$					
τ_{A_2}	0.23	0.42	0.48	0.61	0.81
R_{ee}^{MD} (σ)	8.9 ± 3.5	8.9 ± 3.6	9.0 ± 3.7	9.0 ± 3.6	9.1 ± 3.6
C_{uc}^{SCFT}	0.9	0.8	0.8	0.9	1.0
L_{q*}	9.8 ± 0.2	9.5 ± 0.4	9.5 ± 0.2	9.9 ± 0.2	10.9 ± 0.4
C_{uc}^{MD}	1.1	1.1	1.1	1.1	1.2

Fig. S3 *(a) Snapshot (red beads for A and blue beads for B monomers), (b) A-B isosurface, (c) A-B radial distribution function and (d) A domain structure factor $S_{AA}(q)$ of a melt of $A_1B_1A_2B_2A_3$ pentaBCP chains with $f_A = 0.4$, $\tau_{A_2} = 0.5$, simulated with $\chi N = 0$. The A-B radial distribution function and structure factor are averaged across all sampled frames from three trials.*

In **Fig. S3** we present representative snapshots, the A-B radial distribution function and A domain structure factor $S_{AA}(q)$ of a $A_1B_1A_2B_2A_3$ pentaBCP melt simulated with unbiased MD simulations at $\chi N = 0$. Small A and B domains appear in the chain snapshot (**Fig. S3a**) and the isosurface (**Fig. S3b**); such domains occur due to random fluctuations in the distribution of each bead type as well as the proximity of similar beads created by the chain connectivity. The radial distribution function of A-B contacts is shown in **Fig. S3c** in for mixed melt of $N = 50$ pentaBCP chains. The height of the contact peak is 1.76 ± 0.06 with a 95% confidence interval (that is, $\pm$ two standard deviations). This value is used to distinguish disordered and disordered-microphase separated structures as outlined in **section II.E** of the main text. The A domain structure factor $S_{AA}(q)$ in **Fig. S3d** indicates the degree of microphase separation present even when no thermodynamic incompatibility exists ($\chi N = 0$) between beads of distinct types. The q values corresponding

to the bead diameter (D_{bead}) and the box side length ($L_{boxsize}$) are marked for comparison with the location of peaks in $S_{AA}(q)$.
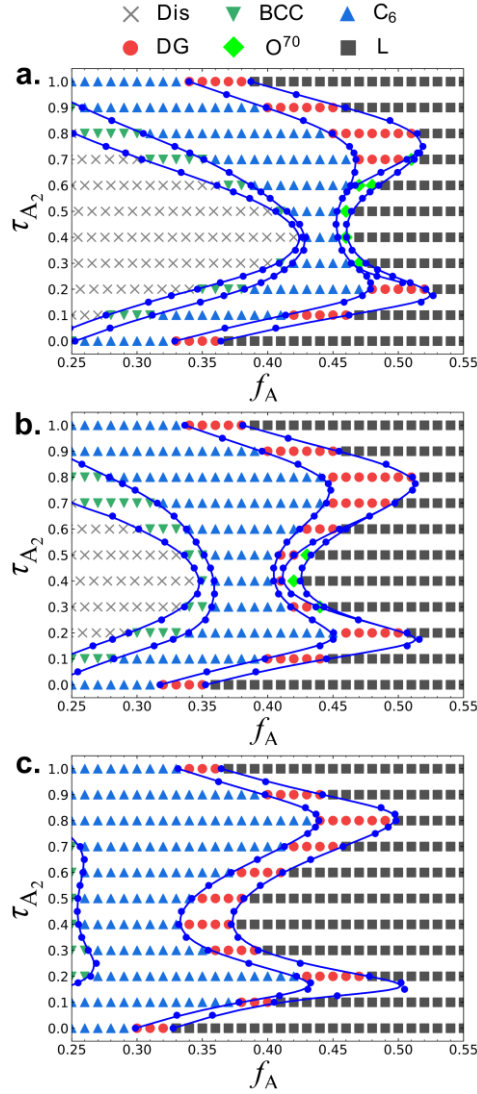

Fig. S4 *The same phase diagrams as those shown in **Fig. 2** in the main manuscript for the $A_1B_1A_2B_2A_3$ pentaBCPs, **with phase boundaries (blue lines)** overlaid on them. The phase boundaries were determined with linear interpolation using the grid points with $\Delta f_A = 0.0025$ and curve-fitting the resolved points with B-splines.*
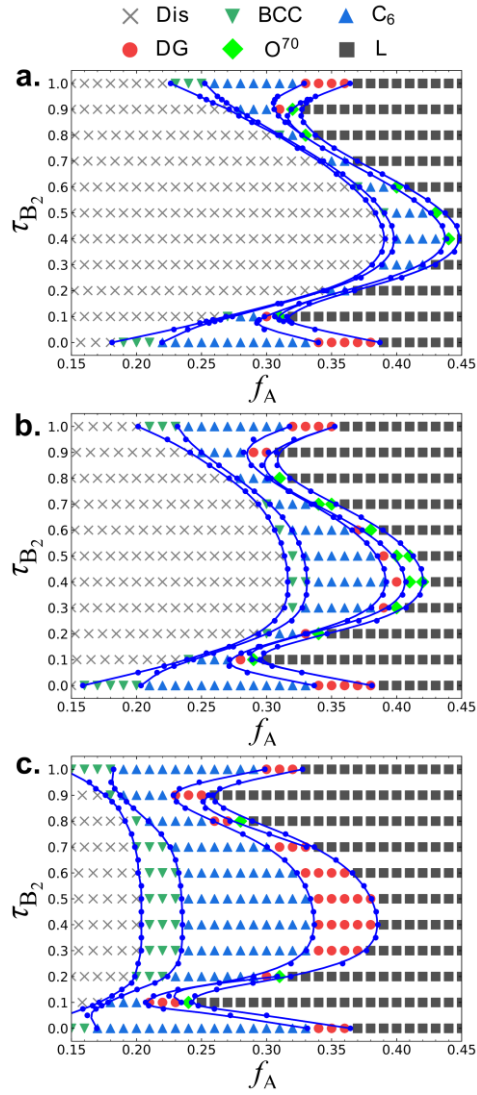
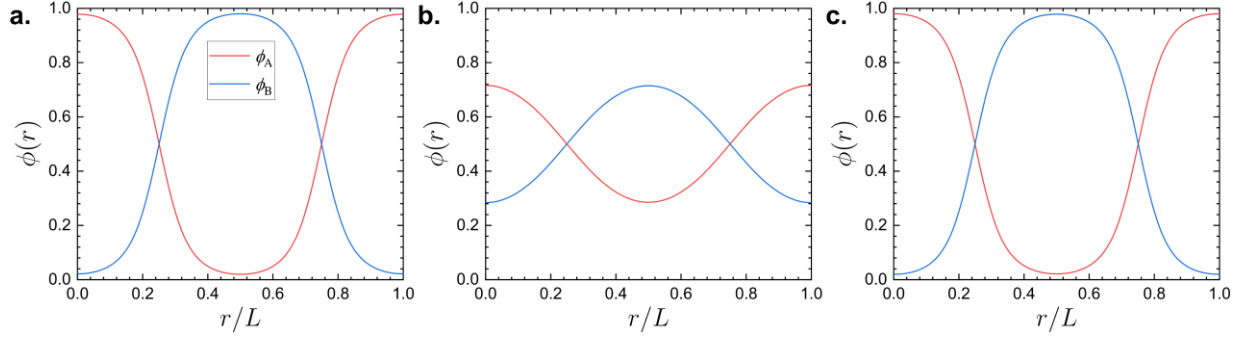**Fig. S5** *Same figure caption as* **Fig. S4** *but for B₁A₁B₂A₂B₃ pentaBCPs.*

Fig. S6 *The spatial SCFT density distributions for the total A blocks ($\phi_{A_1} + \phi_{A_2} + \phi_{A_3}$, red lines) and the total B blocks ($\phi_{B_1} + \phi_{B_2}$, blue lines) for the lamellar phases formed by the (a) ABA triBCP ($\tau_{A_2} = 0.0$), (b) $A_1B_1A_2B_2A_3$ pentaBCPs ($\tau_{A_2} = 0.4$), and (c) BAB triBCP ($\tau_{A_2} = 1.0$) at $\chi N = 35$ and $f_A = 0.5$, identified on the phase diagram in **Fig. 2a** of the main manuscript. The lamellar periods are (a) $L = 1.197b$, (b) $L = 0.715b$, and (c) $L = 1.197b$.*
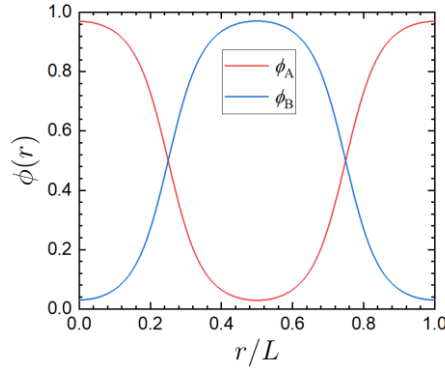

Fig. S7 *The spatial SCFT density distributions for the total A blocks ($\phi_{A_1} + \phi_{A_2} + \phi_{A_3}$, red line) and the total B blocks ($\phi_{B_1} + \phi_{B_2}$, blue line) for the lamellar phases formed by the $A_1B_1A_2B_2A_3$ pentaBCPs at $f_A = 0.5$, $\tau_{A_2} = 0.4$, and $\chi N = 60$, identified on the phase diagram in **Fig. 2c** of the main manuscript. The lamellar period is $L = 0.838b$.*
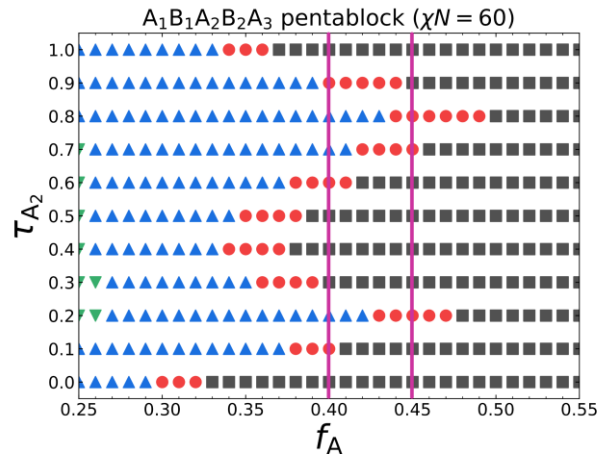
Fig. S8 *The same phase diagram shown in **Fig. 2c** in the main manuscript for the $A_1B_1A_2B_2A_3$ pentaBCPs at $\chi N = 60$, with the two vertical lines ($f_A = 0.40$ and $f_A = 0.45$) overlaid to highlight the reentrant phase transitions.*
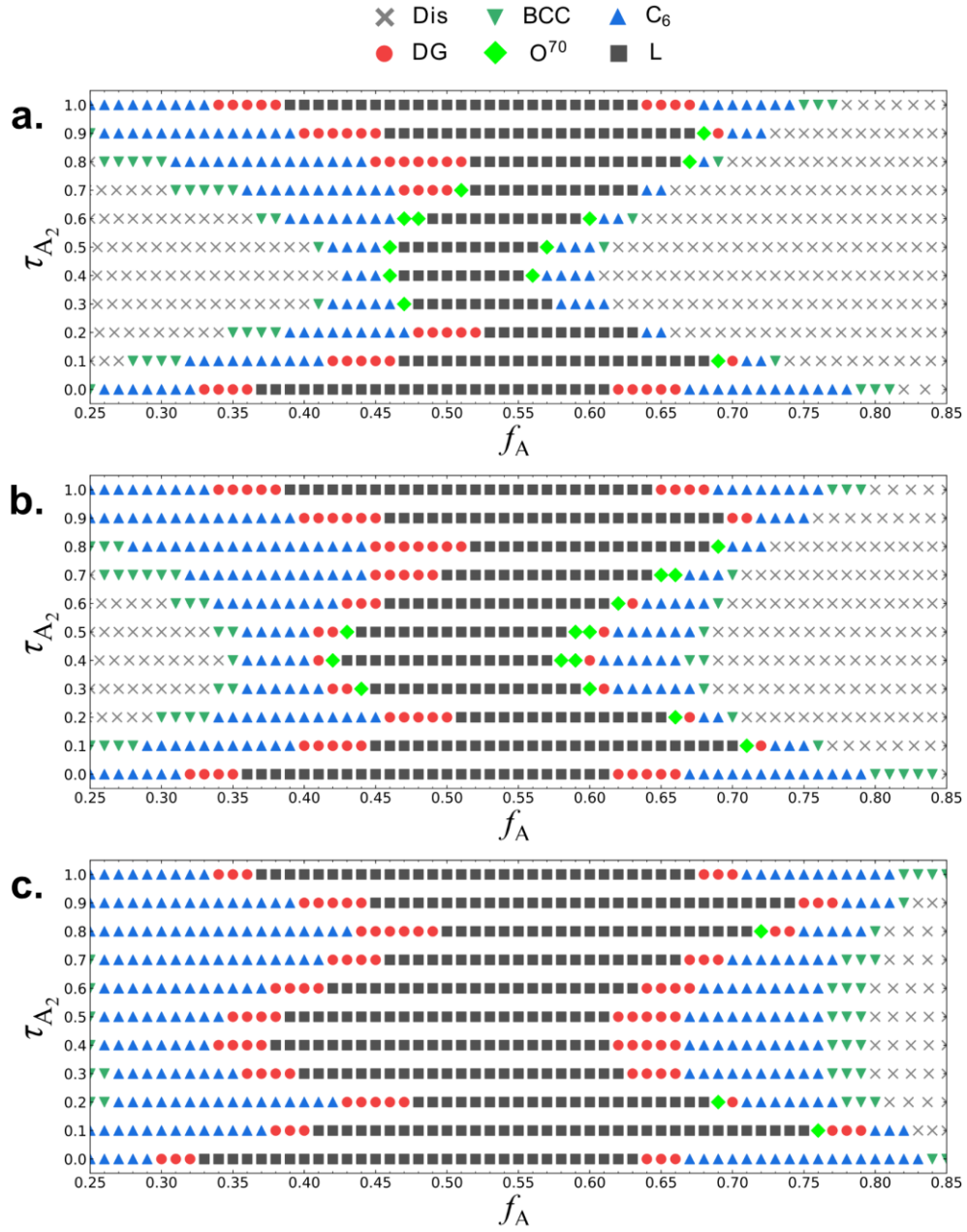
Fig. S9 *The combined phase diagrams of the $A_1B_1A_2B_2A_3$ pentaBCPs and the $B_1A_1B_2A_2B_3$ pentaBCPs in the Fig. 2 and Fig. 3 in the main manuscript, respectively, after redefining the A and B definitions in the $B_1A_1B_2A_2B_3$ pentaBCPs.*

SCFT Calculations for Fraction of Different Chain Conformations

The previous SCFT papers[1-3] present how to compute the fraction of looping and bridging configurations of one block in block copolymers by solving partial partition functions with modified initial conditions defined by Voronoi unit cells. The method requires construction of Voronoi cells within the morphology and propagating the partial partition function (by solving the modified diffusion equation in SCFT) from the initial condition corresponding to the one end of the interest block constrained to a specific Voronoi cell. However, computing the fraction of chain conformations in **Fig. S10** requires propagating the partial partition functions for the three consecutive blocks (i.e., second, third and fourth blocks in the pentaBCP) with a series of different initial conditions, which are not independent as in the previous calculations.[1, 2] Here, instead of evaluating the three blocks, we used a simpler approach by considering only two equal segments of the chain divided by the mid-point of the chain (the mid-point of the middle A block). Both segments have one free end and one junction end, which are denoted by the three green dots in **Fig. S10**. This approach reduces complexity in partial partition function calculations by categorizing the 6 distinct conformations into four conformations (1. *Looping-1* and *Looping-2*, 2. *Hairpin*, 3. *Hybrid-1* and *Hybrid-2*, and 4. *Bridging*), which allows use of independent initial conditions for the partial partition function calculations. The detailed mathematical SCFT formalism is explained as follows. Here, we present the fractions of the ABABA pentaBCP conformations in the L morphology calculated by the SCFT partial partition functions.
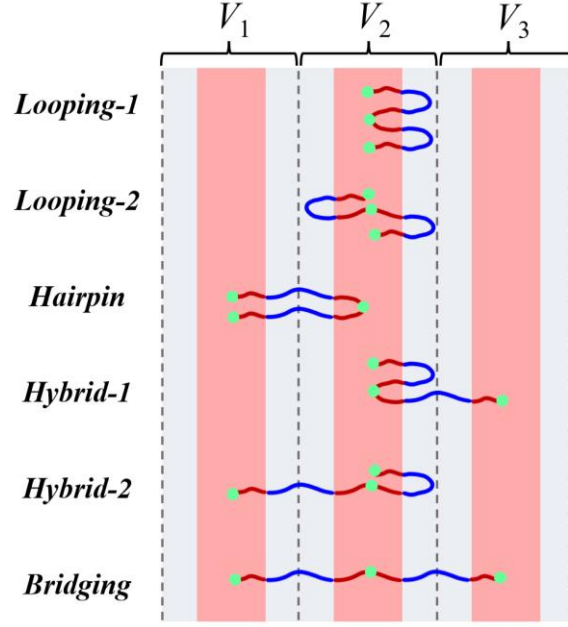
Fig. S10 *Schematics of possible $A_1B_1A_2B_2A_3$ pentaBCP conformations in the lamellar morphology with the three Voronoi unit cells V_1, V_2, and V_3.*

The first step is to determine the Voronoi unit cells in the SCFT morphology, which is straightforward in L morphology. **Fig. S10** illustrates the three Voronoi unit cells (V_1, V_2, and V_3) by which the initial conditions of the partial partition functions corresponding to the two segments will be determined as follows. The initial condition of partial partition function $\bar{q}_n(\mathbf{r}, s)$ with the first free end ($s = 0$) constrained to the nth unit cell is defined as

$$\bar{q}_n(\mathbf{r}, 0) = \begin{cases} 1, & \text{if } \mathbf{r} \in n\text{th Voronoi cell} \\ 0, & \text{otherwise} \end{cases} \tag{1}$$

Similarly, the initial condition of the conjugate partial partition function $\bar{q}_n^{\dagger}(\mathbf{r}, s)$ with the last free end ($s = N$) constrained to the nth unit cell is defined as

$$\bar{q}_n^{\dagger}(\mathbf{r}, N) = \begin{cases} 1, & \text{if } \mathbf{r} \in n\text{th Voronoi cell} \\ 0, & \text{otherwise} \end{cases} \tag{2}$$

With precalculated converged mean field solutions ω_A and ω_B, the two partial partition functions are evaluated by solving the modified **eqns (1)** and **(2)** in the manuscript.

Since the modified partial partition functions $\bar{q}_n(\mathbf{r}, s)$ and $\bar{q}_n^\dagger(\mathbf{r}, s)$ are not periodic, the large simulation cell sizes, which are 8 times the lamellar unit cell sizes, are adopted to remove the finite size effect arising from periodic boundary condition. We confirmed the simulation cell size is large enough with negligible errors in the fraction calculations. We also justified the simulation sizes by confirming that the distribution of the partial partition functions propagated from the initial condition constrained in a Voronoi unit cell remains away from the simulation boundaries ($r = 0$ and $r = L$) as shown in **Fig. S11**.
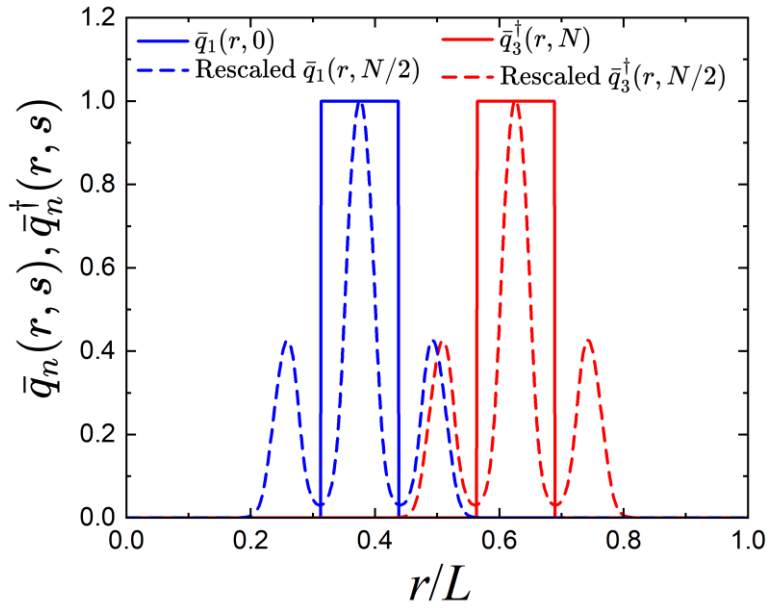

Fig. S11 *The SCFT partial partition functions calculated for the fractions of different chain conformations in **Fig. S10**. The blue and red solid lines are the initial conditions for the partial partition functions constrained to the Voronoi unit cells V_1 and V_3, respectively. The blue and red dashed lines are the distributions of propagated partial partition functions, which are rescaled in q values to present in the same plot.*

Once the partial partition functions are computed, the probability of both free ends and middle point of the chain being in the same Voronoi unit cell (V_2) is obtained by

$$v_{\text{Looping1,2}} = \frac{1}{QV_{\text{cell}}} \int_{V_2 \text{ cell}}^{\square} d\mathbf{r}\, \bar{q}_2(\mathbf{r}, s=N/2)\, \bar{q}_2^{\dagger}(\mathbf{r}, s=N/2) \tag{3}$$

where Q is the total partition function explained in section **II.B.** of the manuscript and V_{cell} are the Voronoi unit cell volume. Since the systems we calculated are in strongly segregated regime ($\chi N = 60$) where most A and B blocks reside in their respective domains, the probability in **eqn (3)** represents the fraction of looping conformations where both free ends and middle point of chain are in the same Voronoi unit cell (*Looping-1* and *Looping-2* in **Fig. S10**).

In the same way, the fraction of hairpin conformation where the middle point and the end points are in different Voronoi unit cell is calculated as follows,

$$v_{\text{Hairpin}} = \frac{1}{QV_{\text{cell}}} \int_{V_2 \text{ cell}}^{\square} d\mathbf{r}\, \bar{q}_1(\mathbf{r}, s=N/2)\, \bar{q}_1^{\dagger}(\mathbf{r}, s=N/2)$$

$$+ \frac{1}{QV_{\text{cell}}} \int_{V_2 \text{ cell}}^{\square} d\mathbf{r}\, \bar{q}_3(\mathbf{r}, s=N/2)\bar{q}_3^{\dagger}(\mathbf{r}, s=N/2) \tag{4}$$

Due to the symmetry in the converged mean field solutions ω_A and ω_B, the computation of the first and the second terms in **eqn (4)** give the same value.

The fraction of hybrid chain conformations (*Hybrid-1* and *Hybrid-2*), where one free end and middle point are in the same Voronoi unit cell and the other end is in the other Voronoi unit cell, is calculated as follows,

$$v_{\text{Hibrid1,2}} = \frac{1}{QV_{\text{cell}}} \int_{V_2 \text{ cell}}^{\square} d\mathbf{r}\, \bar{q}_2(\mathbf{r}, s=N/2)\, \bar{q}_3^{\dagger}(\mathbf{r}, s=N/2)$$

$$+ \frac{1}{QV_{\text{cell}}} \int_{V_2 \text{ cell}}^{\square} d\mathbf{r}\, \bar{q}_3(\mathbf{r}, s=N/2)\bar{q}_2^{\dagger}(\mathbf{r}, s=N/2)$$

$$+ \frac{1}{QV_{\text{cell}}} \int_{V_2 \text{ cell}}^{\square} d\mathbf{r}\, \bar{q}_1(\mathbf{r}, s=N/2)\bar{q}_2^{\dagger}(\mathbf{r}, s=N/2)$$

$$+ \frac{1}{QV_{\text{cell}}} \int_{V_2 \text{ cell}}^{\square} d\mathbf{r} \, \bar{q}_2(\mathbf{r}, s = N/2) \bar{q}_1^\dagger(\mathbf{r}, s = N/2) \tag{5}$$

The symmetry in the mean field solutions and in the pentaBCP architecture makes all terms in the right-hand side of **eqn (5)** have the same value.

Lastly, the fraction of the bridging conformation where all three points are in the different Voronoi unit cells is calculated as follows,

$$v_{\text{Bridging}} = \frac{1}{QV_{\text{cell}}} \int_{V_2 \text{ cell}}^{\square} d\mathbf{r} \, \bar{q}_1(\mathbf{r}, s = N/2) \, \bar{q}_3^\dagger(\mathbf{r}, s = N/2)$$

$$+ \frac{1}{QV_{\text{cell}}} \int_{V_2 \text{ cell}}^{\square} d\mathbf{r} \, \bar{q}_3(\mathbf{r}, s = N/2) \bar{q}_1^\dagger(\mathbf{r}, s = N/2) \tag{6}$$

Again, the symmetry in the pentablock copolymer architecture makes the values of first and the second term in **eqn (6)** same. **Fig. S12**, presents the computed fractions for each conformation at different τ_{A_2} values for ABABA pentaBCP at $f_A = 0.4$ and $\chi N = 60$. The equilibrium phases at each τ_{A_2} in SCFT are L ($\tau_{A_2} = 0.4$), L ($\tau_{A_2} = 0.5$), and DG ($\tau_{A_2} = 0.6$), but we present the fractions calculated in L phase for the comparison with MD simulation results in **Fig. 7** of the main manuscript. Assuming that both loop and hairpin conformations give low R_{ee} values, the hybrid conformations give intermediate R_{ee} values, and bridging conformations give the highest R_{ee} value, the SCFT fraction data can be directly compared with the proportion of each population obtained by MD simulation in **Fig. 7**.
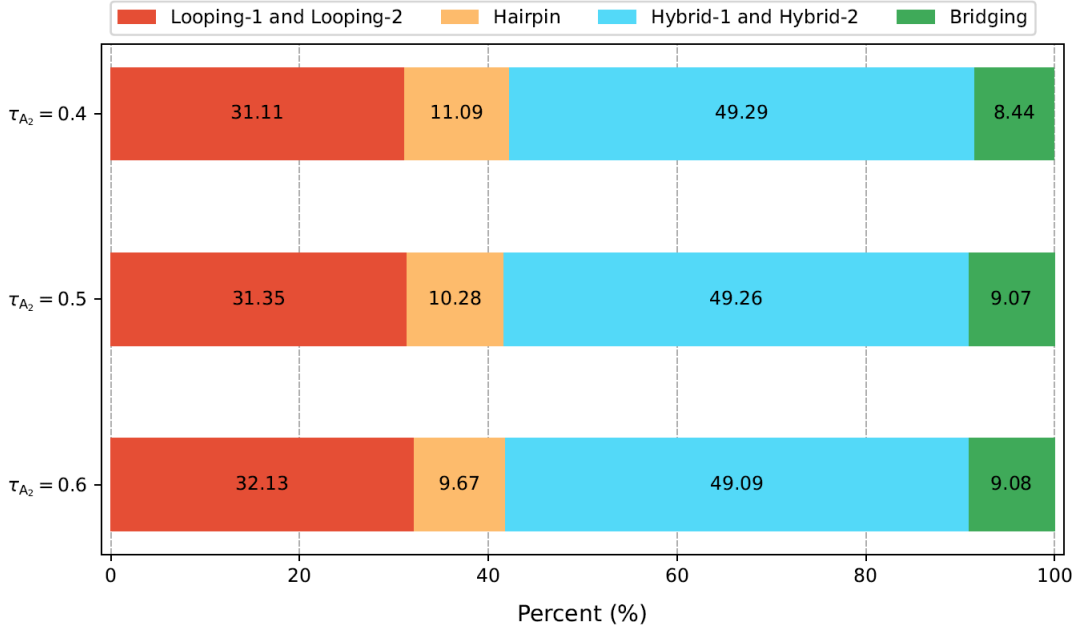
Fig. S12 *Percentage bar charts for the fractions of different chain conformations (obtained from SCFT approach) described in* **Fig. S10**. *The fractions of the $A_1B_1A_2B_2A_3$ pentaBCP conformations in the L morphology are calculated for* $\tau_{A_2} = 0.4, 0.5,$ *and* 0.6 *at* $f_A = 0.4$ *and* $\chi N = 60$.

The SCFT calculations results (**Fig. S12**) give qualitative agreement with the MD simulation data (**Fig. 7d-7f**); the fractions of high end-to-end distance R_{ee} conformation (bridging) are always the smallest, and the fractions of the medium R_{ee} conformation (hybrids) are always the largest. However, there are some differences between SCFT and MD simulation results; in SCFT the fractions of the low R_{ee} conformations (loops and hairpins) and the fractions of the medium R_{ee} conformations (hybrids) are similar with ∼ 40 – 50% while in the MD simulations there are large differences between low R_{ee} fractions (ranging from 27 – 30%) and the medium R_{ee} fractions (∼ 63%). For the low R_{ee} conformations in **Fig. S12**, the hairpin conformation fractions are ∼10% and the looping conformations are the majority conformations with ∼30%, which supports our assumption in **Fig. 7** that the low R_{ee} populations mostly consist of chains with the looping conformations. In addition, the small fractions of high R_{ee} conformation (bridging) in **Fig. S12** support the assumption in the hypothesized conformations in **Fig. 4f-l** of the main manuscript that the possibility of chain conformations with two B blocks bridging can be neglected.
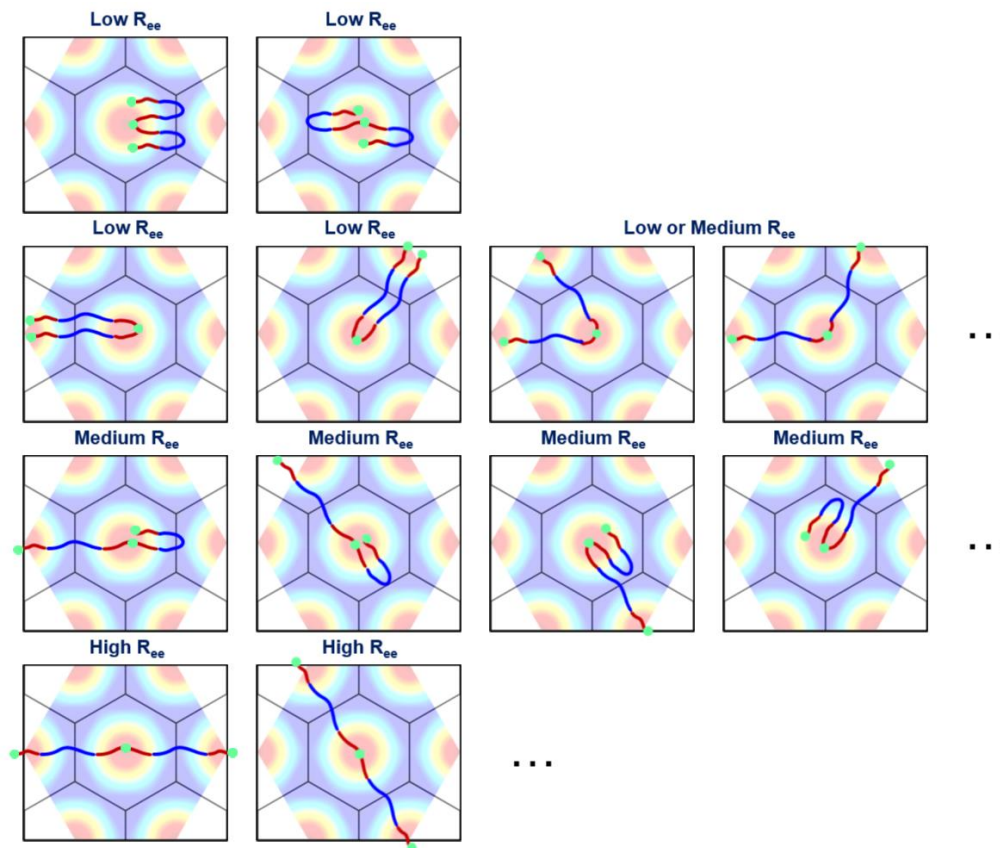
Fig. S13 *Examples of a few of the possible $A_1B_1A_2B_2A_3$ pentaBCP conformations in the C_6 morphology (top view) within the 7 Voronoi unit cells.*

Fig. S13 illustrates a small part of an exhaustive list of chain conformations defined by different Voronoi unit cells in the C_6 morphology. Depending on which Voronoi unit cell the chain ends reside, the chain conformations have different R_{ee} from low to high. Even though some chain conformations in **Fig. S13** have the same probability due to the rotational symmetry in the C_6 morphology, evaluating the chain conformations in SCFT requires enumerating all possible initial conditions belonging to the different Voronoi unit cells, which becomes complicated with complex chain architecture or the number of Voronoi unit cell initial conditions increases as in the C_6 morphology versus L morphology.

In contrast to the above complexities in SCFT calculations, MD simulations provide a straightforward way to evaluate the population of chain conformations by analyzing the distribution of chains from low to high R_{ee}. As shown in **Fig. 7** of the main manuscript, the distribution of R_{ee} can be extracted directly from

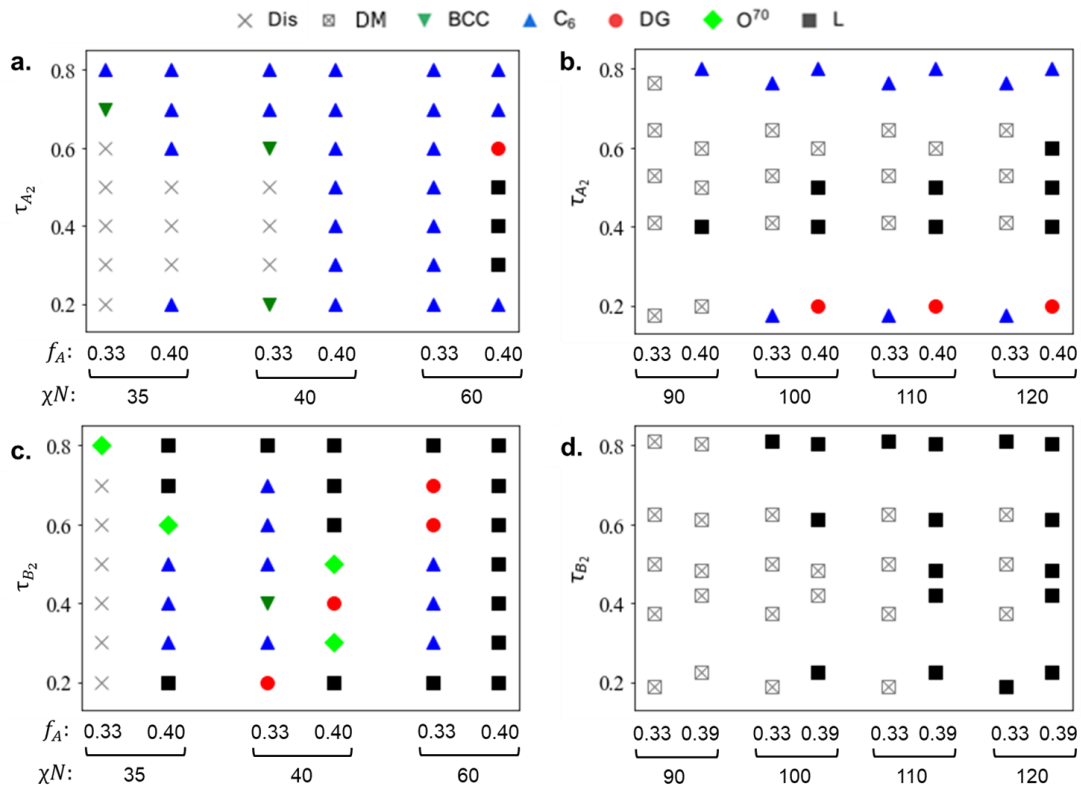sampling the chains in MD simulations while SCFT requires separate calculation for each chain conformation.

Fig. S14 *Comparison of morphologies predicted by (a) SCFT and (b) MD simulation for $A_1B_1A_2B_2A_3$ pentaBCPs and by (c) SCFT and (d) MD simulation for $B_1A_1B_2A_2B_3$ pentaBCPs. Chain designs are chosen to closely match the f_A, τ_{A_2}, and τ_{B_2} values on the phase diagram from SCFT. The legend on top of the plot connects the symbols to the morphologies. The schematic representation of each ordered morphology can be found in* **Table 1** *of the main paper. We note again that the "disordered microphase" (DM) occurs when the height of the contact peak of the A-B radial distribution function of a given melt is $\leq 1.76 \pm 0.06$ without the formation of an ordered morphology.*

The morphologies found to be the energy minimum in SCFT at χN = 35, 40, and 60 for chains with f_A = 0.33 and 0.4 and $\tau_{A \text{ or } B_2}$ from 0.2 to 0.8 are shown in the left column in **Fig. S14**. The morphologies observed in MD simulations at χN = 90, 100, 110, and 120 for chains with $f_A \sim 0.33$ and 0.4 and $\tau_{A \text{ or } B_2} \sim$ 0.2, 0.4, 0.5, 0.6, and 0.8 are displayed on the right column in **Fig. S14**. The SCFT calculations predict

ordered morphologies at $\chi N = 60$, while for MD simulations ordered morphologies only show up at higher χN. This discrepancy in the ODT in SCFT vs. MD simulation is well-documented in the literature and is attributed to the density fluctuations which are present in the particle-based simulations but absent in the SCFT calculations.[4-8] These fluctuations have the effect of increasing $(\chi N)_{ODT}$ as well as increasing the thermodynamic favorability of high curvature phases like DG near the ODT.[6, 7] Mostly, there is good correspondence between the sequence of morphologies observed with SCFT calculations and MD simulations with increasing $\tau_{A \text{ or } B_2}$ for the highest χN for each method ($\chi N = 60$ for SCFT and $\chi N = 120$ for MD simulation). We will discuss the comparison of results from SCFT and MD simulations in detail next.

For $A_1B_1A_2B_2A_3$ pentaBCPs at $\chi N = 60$ with $f_A \sim 0.33$, SCFT (**Fig. S14a**) predicts the C_6 phase to be formed at all values of τ_{A_2}; in contrast, in MD simulations (**Fig. S14b**), only two of the five simulated designs with the same sequence and f_A formed ordered morphologies at $\chi N = 120$ and that ordered morphology is C_6.

For $A_1B_1A_2B_2A_3$ pentaBCPs at $\chi N = 60$ with $f_A \sim 0.4$ as τ_{A_2} is increased from 0.2 to 0.8 SCFT (**Fig. S14a**) predicts morphologies $C_6 \rightarrow L \rightarrow DG \rightarrow C_6$. With MD simulations (**Fig. S14b**) we see a similar reentrant sequence $DG \rightarrow L \rightarrow C_6$ at $\chi N = 120$. We note that within the three trials of MD simulations τ_{A_2} = 0.2 and 0.8, we observed both C_6 and DG. We use additional tests as described to conclude that these morphologies are similar in free energy for these designs.

For the $B_1A_1B_2A_2B_3$ pentaBCPs at $\chi N = 60$ with $f_A \sim 0.33$, SCFT (**Fig. S14c**) predicts the sequence $L \rightarrow C_6 \rightarrow DG \rightarrow L$, while MD simulations (**Fig. S14d**) predict the sequence $L \rightarrow DM \rightarrow L$ at $\chi N = 120$.

For the $B_1A_1B_2A_2B_3$ pentaBCPs at $\chi N = 60$ with $f_A \sim 0.4$, both SCFT (**Fig. S14c**) and MD simulations (**Fig. S14d**) predict the L morphology at all values of τ_{B_2} that we studied.

We note that for systems with $f_A \sim 0.4$, both pentaBCP sequences were fully ordered at $\chi N = 120$ and ordered at lower χN than the pentaBCPs with $f_A \sim 0.33$, in accordance with the trends in the SCFT data, despite the discrepancy between both methods in the χN required for ordering.

When multiple trials of a regular MD simulations show possibility of different morphologies (e.g., occurrences of C_6 and DG) or if there is a clear disagreement in the ordered morphology between SCFT and MD simulations, we use our newly developed high-throughput computational framework **RAPSIDY** - Rapid Analysis of Polymer Structure and Inverse Design strategY - described next.

<u>R</u>apid <u>A</u>nalysis of <u>P</u>olymer <u>S</u>tructure and <u>I</u>nverse <u>D</u>esign strateg<u>Y</u> (RAPSIDY)

The RAPSIDY procedure allows us to initialize MD simulations using configurations where chains with a specific polymer design are pre-placed within canonical morphologies to directly evaluate stability of a particular phase (e.g., double gyroid) for that polymer design without having to use slow, global optimization procedures such as simulated annealing used in traditional MD. Our methodology allows us to rapidly screen the stability of canonical phases (e.g., lamellar, double gyroid, hexagonal-packed cylinders) or non-canonical phases (e.g., user defined morphologies) with a two orders of magnitude acceleration in computation time compared to traditional MD. We also apply this accelerated stability analysis to address the long-standing problem of incommensurability, which distorts the self-assembled structure in BCP melts and is challenging to prevent. In the following section, we briefly summarize the initialization process but encourage readers to refer to our separate publication for details.[9]

Chains within a random melt are biased into conformations that form a desired morphology using an external potential, V_{ext}, defined by a known, reference density field, φ^{ref}. The reference density field is a discretized 3D function, $\varphi^{ref} = \varphi^{ref}(x, y, z)$, which defines the number density of each species at each mesh point. This guiding field is inspired by previous work of Nowak and Escobedo,[10] Müller and Daoulas[11] and Lequieu [12] who have used similar forms.

$$V_{ext} = A \sum_{i}^{M} (\varphi_i - \varphi_i^{ref})^2 \tag{7}$$

Here, φ_i and φ_i^{ref} refer to the density of the simulation and reference field, respectively, at mesh point i, M is the total number of mesh points, and A is a user-defined scaling constant. When the simulation density is far away from the target morphological density field, the system potential energy is heavily penalized, but as the system approaches the target morphological density, then the field tends to 0. The scaling constant, A, is chosen such that the forces exerted on the beads are comparable in magnitude to the forces exerted by the existing bonded and non-bonded interactions for numerical stability. In our case, we found $A = 100$ to be a reasonable tradeoff between numerical stability and equilibration speed. During this initialization

process, we also modify the non-bonded Lennard Jones (LJ) potential of the system by capping to maximum pairwise energy to the value obtained at $0.8d$. This modified non-bonded potential allows beads and chains to overlap which in turn significantly accelerates the initialization process by allowing chain movements that are unphysical with a traditional LJ potential. The combination of the external guiding potential coupled with force-capped LJ potential allows all chains to settle within their desired morphologies within ~10^3 timesteps. After chains settled within their desired morphologies, the external potential and force-capping is turned off to allow the system and the chains to naturally evolve to their (global) free energy minima. We compare the scattering profiles of the morphology at the beginning and end of equilibration to determine if the biased morphology was retained. Reference density fields for the canonical phases tested (L, C_6, and DG) are defined from their mathematical structure and their respective derivations can be found in our corresponding publication.[9]

RAPSIDY also addresses one of the long-standing challenges associated with conducting periodic MD simulations of block copolymers where the box size needs to be an integer multiple of the periodicity of the stable morphology which is not known *a priori*. Our future publication presenting RAPSIDY will discuss the various applications of this approach. Here, we present one example application of RAPSIDY to determine the equilibrium morphology of a given chain design and thereby resolve the discrepancy between predictions from SCFT calculations and MD simulations or variability in morphology predictions from multiple trials of the same system.
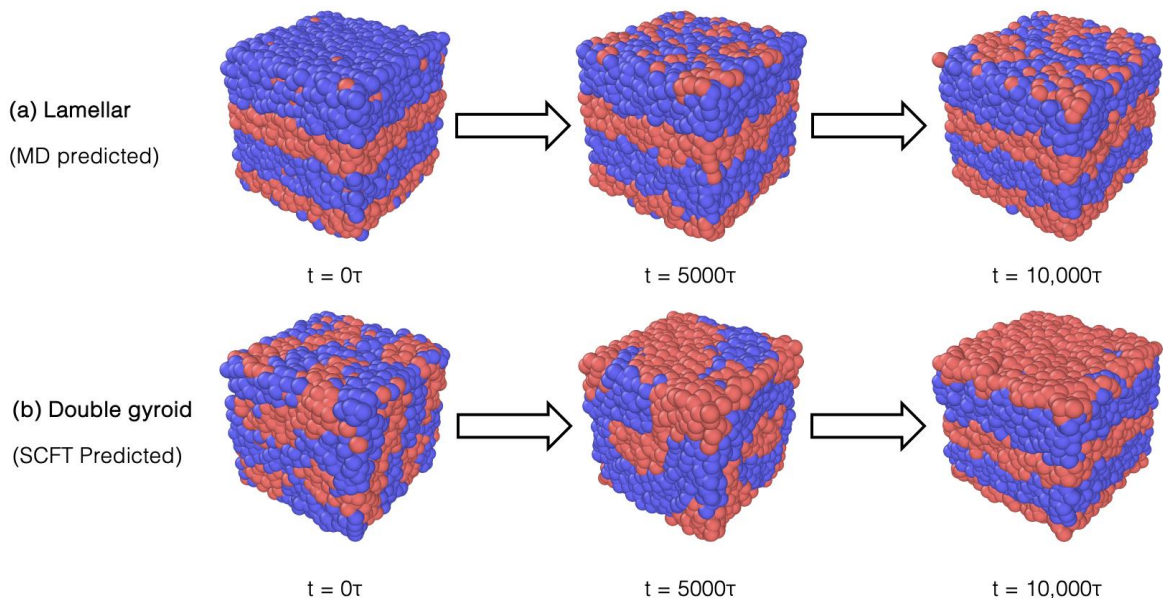
Fig. S15 *Snapshots of (a) lamellae (L) and (b) double gyroid (DG) trajectories initialized using biased MD for $A_1B_1A_2B_2A_3$ pentaBCP with f_A= 0.4 and τ_{A_2} = 0.6 at χN =120 (red denotes A and blue denotes B). The system initialized as a L structure (as predicted by MD simulations) rapidly equilibrates and remains in the initial morphology after 10,000τ. However, when the system is initialized as DG (as predicted from SCFT), the system transitions towards a L morphology with identical domain spacing (~10d) to that obtained from (a) and from traditional (unbiased) MD. This confirms that with particle-based simulations for this design, the L morphology is more stable than DG morphology.*

For $A_1B_1A_2B_2A_3$ pentaBCP with f_A= 0.4 and τ_{A_2} = 0.6, the SCFT prediction and MD simulation prediction at the highest χN values do not agree; SCFT predicts DG while MD simulation predicts L. In **Fig. S15** we show simulation snapshots over the course of 10,000τ with RAPSIDY method starting with L and DG morphologies for polymer design f_A= 0.4 and τ_{A_2} = 0.6 at a high segregation strength of χN = 120. The system initiated as a L structure rapidly equilibrates and remains within the initial prescribed morphology after 5,000τ and 10,000τ. However, the system initiated as DG quickly transitions away from DG (after 5,000τ) towards an L morphology (after 10,000τ) with identical domain spacing (~10d) to that obtained by the previous biased initiation and traditional MD. The above observations are consistent over three trials and shows that DG is not stable (or L is more stable than DG) even at a high segregation strength of χN = 120. The L morphology is also stable at lower segregation strengths, including χN = 90, 100, and 110. For all other sequence designs (f_A = 0.4, τ_{A_2} = 0.2, 0.4, 0.5, 0.8) at χN = 120, we found that the morphologies predicted by SCFT and MD were stable over 10,000τ after biased initialization; this includes both the C_6

and DG morphologies predicted by SCFT and MD, respectively, for the pentaBCP with $\tau_{A_2} = 0.2$. Our rapid initialization procedure suggests that discrepancies between SCFT and traditional MD predicted phases are likely not due to kinetic trapping by our annealing protocol but rather by fundamental differences between particle-based and mean-field-based approaches.

Next, we apply this RAPSIDY procedure to evaluate the stability of each canonical morphology for the melts that regular MD simulations predict to form DM morphology (**Fig. S14**) at $90 \leq \chi N \leq 120$.
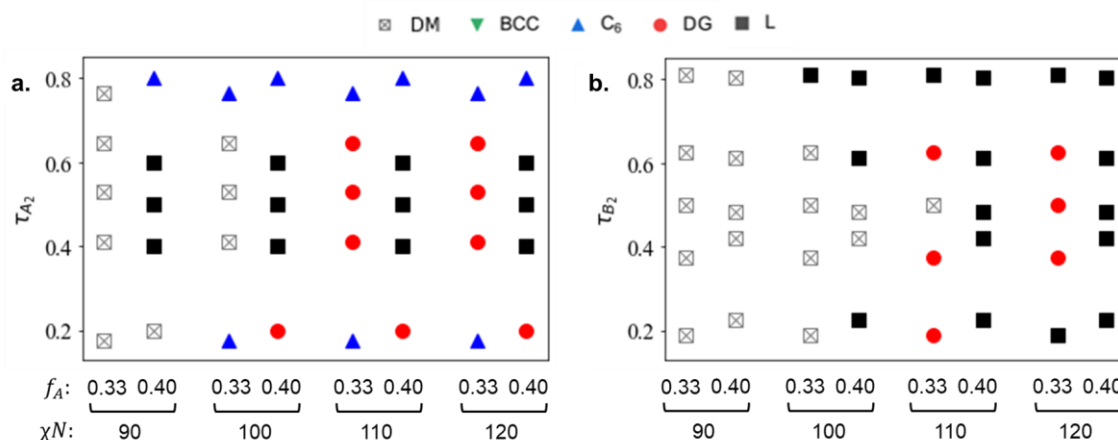

Fig. S16 *Morphologies for melts of (a) $A_1B_1A_2B_2A_3$ pentaBCPs and (b) $B_1A_1B_2A_2B_3$ pentaBCPs. To achieve the above phase diagrams, we started with pentaBCP melts in the DM phase as predicted by unbiased MD (**Fig. S14b** and **Fig. S14d**) and using RAPSIDY tested to see if a stable ordered morphology formed; if an ordered morphology was formed, then we replace the DM symbol with that order morphology symbol in the phase diagram. The final "stable" phase diagrams are shown above.*

In **Fig. S16** we present the complete set of equilibrium morphologies found for pentaBCPs melts using RAPSIDY and our unbiased MD simulations as described in the caption of the figure. While several chain designs remained DM at $\chi N = 110$ and even $\chi N = 120$ in all three trials of unbiased MD simulation, all but one formed an ordered morphology at $\chi N = 110$ and each was ordered at $\chi N = 120$ at the end of RAPSIDY. We note that several of melts which unbiased MD predicted to have the DM morphology, biased MD later identified DG to be the equilibrium.

As we previously observed from the unbiased MD simulations of pentaBCP of sequence $A_1B_1A_2B_2A_3$, $f_A = 0.4$, and $\tau_{A_2} = 0.2$ or 0.8, the C_6 and DG morphologies are degenerate for many chain designs. We also

found some of the DM morphologies for these pentaBCP melts in unbiased MD to at least partially consist of perforated lamellae and the melts initialized as lamellae in RAPSIDY rapidly formed perforated lamellae. The perforated lamellae phase is known to be a stable or long-lasting metastable morphology in BCP melts, but it is also frequently a metastable precursor to a stable DG structure.[5, 13-15]
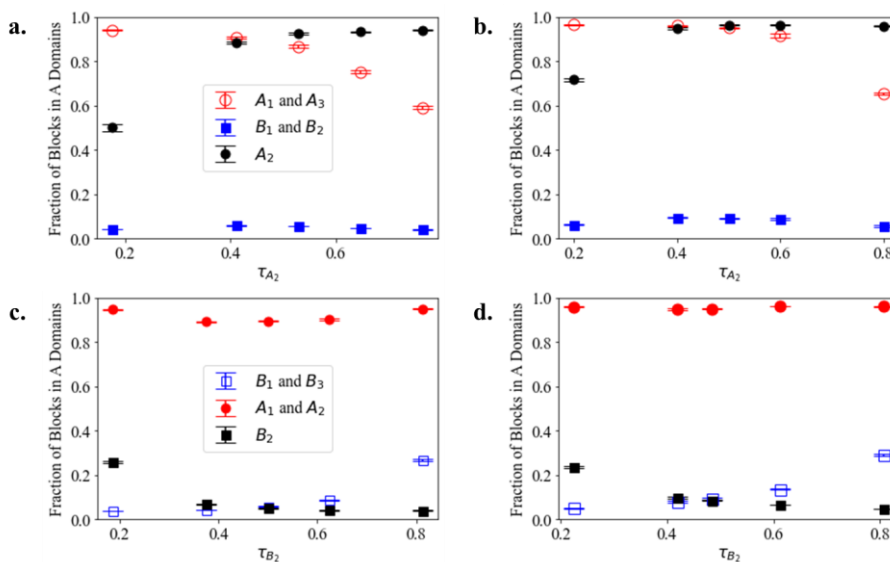

Fig. S17 *The fractions of the end A blocks, A_1 and A_3 (open red circle), the B blocks, B_1 and B_2 (filled blue squares), and the middle A block, A_2 (filled black circles) in A domains, of $A_1B_1A_2B_2A_3$ pentaBCPs with (a) $f_A = 0.33$ and (b) $f_A = 0.4$ (repeated from **Fig. 5**), and the fractions of the end B blocks, B_1 and B_3 (open blue squares), the A blocks A_1 and A_2 (filled red circles), and the middle B block, B_2 (filled black squares) in A domains, of $B_1A_1B_2A_2B_3$ pentaBCPs with (c) $f_A = 0.33$ and (d) $f_A = 0.4$, at several τ_{A_2} from MD simulation at $\chi N = 120$. The plotted fraction and error bars represent the average and standard deviation of the computed fractions from each sampled frame from all three trials.*
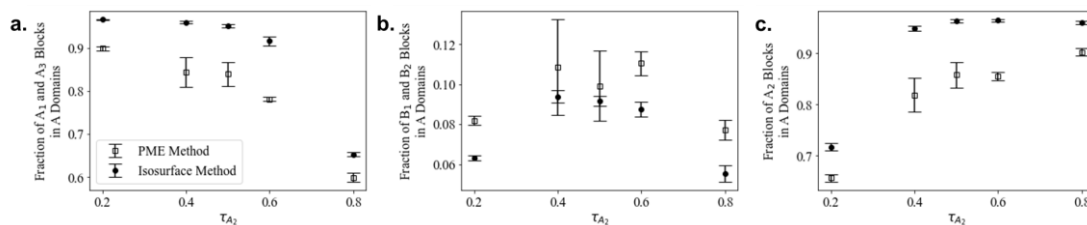

Fig. S18 *The fractions of (a) the end A blocks, A_1 and A_3, (b) the B blocks, B_1 and B_2, and (c) the middle A block, A_2, in A domains, of $A_1B_1A_2B_2A_3$ pentaBCPs with $f_A = 0.4$ and several τ_{A_2} from MD simulation at*

$\chi N = 120$. *The A and B domains are determined with the particle mesh Ewald (PME) method as well as with isosurfaces drawn with a Gaussian density mesh, and the fraction is found as the proportion of each block's constituent beads in the A domain. The plotted fraction and error bars represent the average and standard deviation of the computed fractions from each sampled frame from all three trials.*
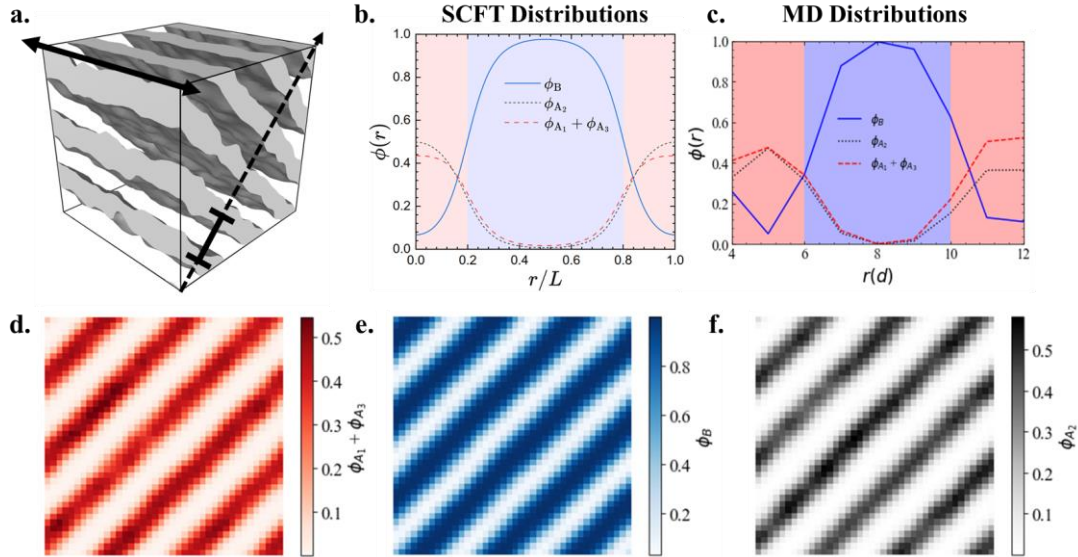

Fig. S19 *The same isosurface snapshot and one- and two-dimensional volume fraction distributions as in* **Fig. 6** *for the $A_1B_1A_2B_2A_3$ pentaBCP melt with $f_A = 0.4$ and $\tau_{A_2} = 0.5$ at $\chi N = 120$. The one-dimensional distributions are sampled within a center-to-center interval (solid line segment with end marks) of a diagonal plane orthogonal to the lamellae (dashed line) and spatially averaged across the plane in the direction of the solid arrow. They are plotted against the distance r from the origin along the dashed arrow. The two-dimensional distributions are averaged along the solid arrow. The volume fraction distributions across the simulation volume are averaged between all sampled frames across three trials.*
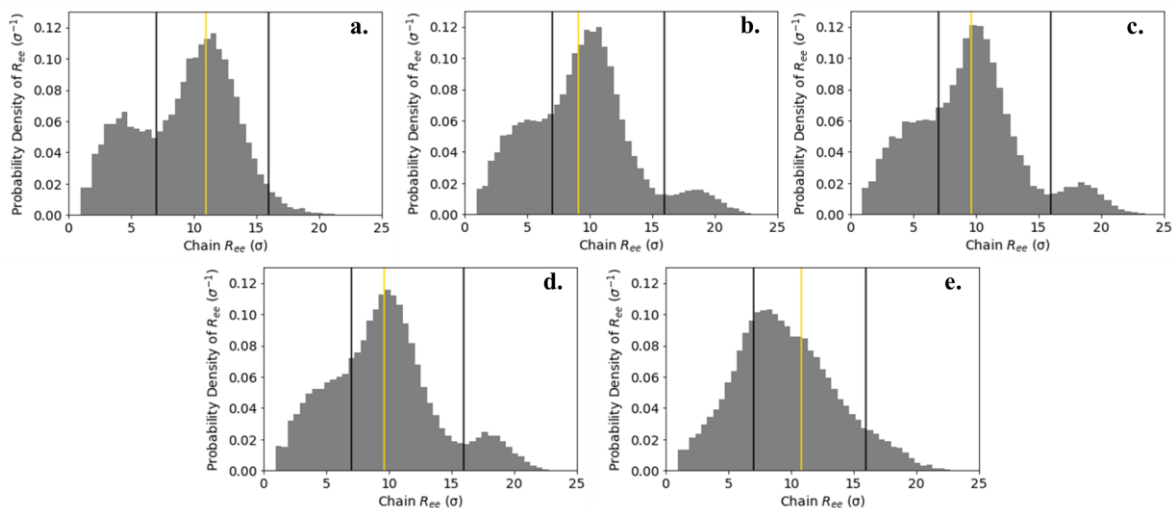
Fig. S20 *Probability density histograms of the end-to-end distance R_{ee} of $A_1B_1A_2B_2A_3$ pentaBCP at $\chi N = 120$ with $f_A = 0.4$ and (a) $\tau_{A_2} = 0.2$, (b) $\tau_{A_2} = 0.4$, (c) $\tau_{A_2} = 0.5$, (d) $\tau_{A_2} = 0.6$, and (e) $\tau_{A_2} = 0.8$. The histograms are divided at $R_{ee} = 7d$ and $16d$ (black vertical line). The real-space distance (L_{q*}) corresponding to the major peak in $S_{AA}(q)$ sampled for each pentaBCP design from the second set of simulations is highlighted (gold vertical line).*

References

1. M. W. Matsen and R. B. Thompson, *J. Chem. Phys.*, 1999, **111**, 7139-7146.
2. F. Drolet and G. H. Fredrickson, *Macromolecules*, 2001, **34**, 5317-5324.
3. R. K. W. Spencer and M. W. Matsen, *Macromolecules*, 2017, **50**, 1681-1687.
4. F. S. Bates, M. F. Schulz, A. K. Khandpur, S. Förster, J. H. Rosedale, K. Almdal and K. Mortensen, *Faraday Discuss.*, 1994, **98**, 7-18.
5. T. M. Beardsley and M. W. Matsen, *J Chem Phys*, 2021, **154**, 124902.
6. M. W. Matsen, T. M. Beardsley and J. D. Willis, *Phys Rev Lett*, 2023, **130**, 248101.
7. M. W. Matsen, T. M. Beardsley and J. D. Willis, *Physical Review Materials*, 2023, **7**.
8. O. N. Vassiliev and M. W. Matsen, *The Journal of Chemical Physics*, 2003, **118**, 7700-7713.
9. V. Liao, T. Myers and A. Jayaraman, *In preparation*, 2024.
10. C. Nowak and F. A. Escobedo, *J Chem Theory Comput*, 2018, **14**, 5984-5991.
11. M. Muller and K. Daoulas, *J Chem Phys*, 2008, **128**, 024903.
12. J. Lequieu, *J Chem Phys*, 2023, **158**.
13. E. W. Cochran, C. J. Garcia-Cervera and G. H. Fredrickson, *Macromolecules*, 2006, **39**, 2449-2451.
14. G. Fredrickson, *The Equilibrium Theory of Inhomogeneous Polymers*, 2005.
15. D. A. Hajduk, P. E. Harper, S. M. Gruner, C. C. Honeker, G. Kim, E. L. Thomas and L. J. Fetters, *Macromolecules*, 2002, **27**, 4063-4075.